



## Invited Research Article

# Characterization of the shallow structure of El Tatio geothermal field in the Central Andes, Chile using transient electromagnetics

Daniela Montecinos-Cuadros<sup>a,b,\*</sup>, Daniel Díaz<sup>a,b</sup>, Pritam Yogeshwar<sup>c</sup>, Carolina Munoz-Saez<sup>b,d</sup>

<sup>a</sup> Departamento de Geofísica, Universidad de Chile, Blanco Encalada 2002, Santiago, Chile

<sup>b</sup> Centro de Excelencia en Geotermia de Los Andes, Plaza Ercilla 803, Santiago, Chile

<sup>c</sup> Institute of Geophysics and Meteorology, University of Cologne, Albertus-Magnus Platz, 50923 Cologne, Germany

<sup>d</sup> Departamento de Geología, Universidad de Chile, Plaza Ercilla 803, Santiago, Chile

## ARTICLE INFO

## Article history:

Received 5 March 2020

Received in revised form 26 January 2021

Accepted 3 February 2021

Available online 8 February 2021

## Keywords:

Geothermal field

Transient electromagnetic

Electrical resistivity

Geothermal manifestation

El Tatio

## ABSTRACT

This study presents the first high resolution geophysical survey conducted in The El Tatio geothermal field, northern of Chile, focused on the detection of shallow subsurface structures and identification of ascending fluid pathways. TEM data was collected along 5 profiles crossing the two main geothermal basins (Upper and Middle Basin) to obtain an electrical resistivity model up to 200 m depth. The models show important structures that allowed us to improve the conceptual model of the field connecting these geophysical observations with the geology and the geochemistry of the area. We found a shallow (<60 m) high conductivity layer in all profiles. This layer was interpreted as a shallow aquifer of thermal water, which is probably the water supplier of surface manifestations. In the Upper Basin a main permeable zone allows the ascent of fluids from deep aquifers to the shallower one, and a structure that probably act as impermeable geological barrier that forces the fluids to ascend has been detected. In the Middle Basin fluid ascent zones are less clear than in the Upper Basin but it is possible to observe areas of lower resistivity that could be associated with higher permeability.

© 2021 Elsevier B.V. All rights reserved.

## 1. Introduction

The El Tatio geothermal field is located in the Chilean Altiplano at an elevation of 4200 m above sea level (Fig. 1). It is the largest geyser field in the southern hemisphere and the third largest in the world (approximately 10% of the geysers in the world), covering more than 30 km<sup>2</sup> and containing more than two hundred active geothermal manifestations such as: geysers, perpetual spouters, fumaroles, hot spring pools and mud-pools (e.g., Glennon and Pfaff, 2003; Munoz-Saez et al. 2018).

Systematic exploration of El Tatio began around 100 years ago with geological studies of the geothermal potential in the area (Tocchi 1923). However, today the internal structure and physical processes controlling fluid flow at El Tatio are still poorly understood. In the 1960's and 1970's 13 deep drillings between a depth of 571 m and 1816 m were conducted and the first local geological maps were obtained (Lahsen and Trujillo 1976). Other studies in the 1970's included geochemical analysis (Cusicanqui 1975; Giggenbach 1978) and geophysical imaging using Vertical Electrical Soundings (Lahsen and Trujillo 1976). In the last two decades, new studies were conducted to understand the large-scale dynamics of the geothermal area (e.g., Cortecci et al. 2005; Glennon and Pfaff, 2003; Lucchi et al. 2009; Mourgues, 2017; Munoz-Saez et al.

2015, 2018; Tassi et al. 2010; Cumming et al. 2002; Ardid et al. 2019; Figueroa 2019). Most of these previous studies were on a regional scale, providing insights into the subsurface water flow, possible geothermal heat source, and electrical resistivities at kilometer scale. However, they did not address the local subsurface structure of the El Tatio geothermal field.

The conceptual models of the geothermal field have been mainly based on geochemical data and information from the wells (e.g., Giggenbach 1978; Munoz-Saez et al. 2018). Geothermal wells (Fig. 1) identified two permeable zones at different depths forming geothermal aquifers confined by relatively impermeable rock formations (e.g., Cusicanqui 1975; Giggenbach 1978; Lahsen and Trujillo 1976). According to the geothermometry, the temperature of the deepest reservoir is ~230 °C, and the heat flow of the system is greater than 150 MW (Munoz-Saez et al. 2018). The isotopic signature of the thermal waters suggested that snowmelt from the mountains, located >15 km to the east of El Tatio at an elevation of >5000 m, recharge the aquifers through a deep fault system (Giggenbach 1978; Munoz-Saez et al. 2018). The surface water geochemistry and isotopic composition indicated that regional meteoric water interacts with the surrounding rock in the geothermal reservoir, before ascending to the surface as

\* Corresponding author at: Departamento de Geofísica, Universidad de Chile, Blanco Encalada 2002, Santiago, Chile.  
E-mail address: [danielamontecinos@ug.uchile.cl](mailto:danielamontecinos@ug.uchile.cl) (D. Montecinos-Cuadros).

boiling water (e.g., Cusicanqui 1975; Giggenbach 1978; Cortecci et al. 2005; Munoz-Saez et al. 2018). The lack of tritium in the surface thermal waters indicates residence times of >60 years for the water in the reservoir (Cortecci et al. 2005; Munoz-Saez et al. 2018). Local meteoric water accumulated in a shallow aquifer (Munoz-Saez et al. 2018) reached the surface and created the existing wetlands in the area (Fig. 1). During the ascent, the thermal waters were mixed in different proportions with this local meteoric water (Giggenbach 1978). Those previous studies provided good explanations about the origin and evolution of the ascending fluids, however the subsurface structures that control the pathways of the fluids have not been well defined.

There have been limited geophysical imaging studies at El Tatio, and most that have been done focused on regional scales. Some magnetotelluric soundings were collected near the main volcanic centers in the area (Cumming et al. 2002; Figueroa 2019), and these data produced electrical resistivity images which verified the existence of deep aquifers as well as confining impermeable layers. The overall objective of this study is to improve the existing conceptual model using high resolution geophysical data from the main basins and identify the subsurface fluid pathways. It is the first geophysical survey which focuses on shallow depths (< 200 m) on a local scale around the geothermal manifestations and sinter hydrothermal deposits, which typically have a high electrical resistivity (Munoz-Saez et al. 2016).

The loop source Transient Electromagnetic method (TEM) is widely used for imaging shallow subsurface structures related to groundwater and salinization problems (e.g., Fitterman and Stewart 1986; Ruthsatz et al. 2018), sedimentary basin studies (Danielsen et al. 2003; Yogeshwar and Tezkan 2017), general geomorphological studies, and

environmental and engineering studies (cf. Tezkan 1999; Goldman et al. 1994). TEM is also a reliable method for determining the subsurface structure and the composition in volcanic and geothermal areas (e.g., Martínez-Moreno et al. 2016; Arnason et al., 2010; Cumming and Mackie 2010; Kajiwara et al. 2000; Goto and Johmori 2011; Jousset et al. 2011; Descloitres et al. 1997; Dickey 2018; Bouligand et al. 2019; Gresse et al. 2017; Lévy et al. 2019). We collected dense TEM data along five profiles in order to derive the electrical resistivities of the subsurface beneath El Tatio geothermal field. The models are derived from applying 1D inversion techniques. Since the resistivity structure varies significantly along the profile, we also performed a 2D modeling analysis to verify the structures and the interpretation.

## 2. Background

### 2.1. Geology and hydrogeology

The El Tatio geothermal field is located in northern Chile (22.32° N, 68.02° W, Fig. 1) and is one of the surface expressions of the ongoing magmatic activity of the Altiplano-Puna Volcanic Complex (APVC) (e.g., De Silva et al. 1994). The surface geothermal activity at El Tatio began ~27,000 years ago and it has been continuous since (Munoz-Saez et al. 2020). The El Tatio geothermal area is bounded by Pliocene - Pleistocene volcanic rocks called the Serrania Tucle-Lucero horst in the west, while no clear boundary is exposed towards the east. Probably, the east boundary is located in the Pleistocene Volcanic Group also called El Tatio, which has a horizontal width of ~7 km. The strong topographic change between the Serrania Tucle-Lucero and the El Tatio

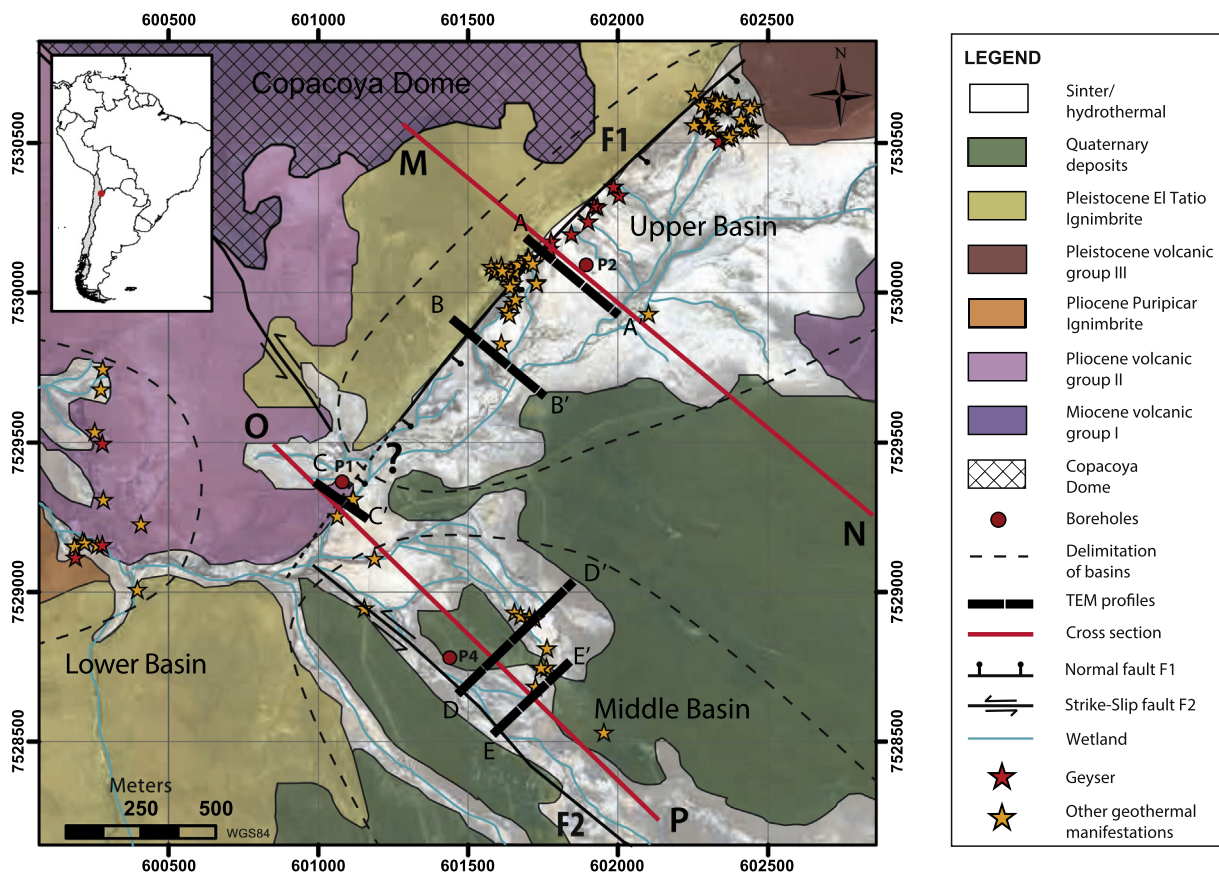


**Fig. 1.** Simplified geological map of El Tatio geothermal field. Dotted lines show the approximate extent of the Upper, Middle and Lower basins; red stars are the location of geysers and yellow stars are other geothermal manifestations (Munoz-Saez et al. 2018); red circles indicate boreholes; blue line represents zones of wetland; thick black lines show TEM profiles; and red lines are the cross sections of the conceptual models (Fig. 6). Geology and main faults (F1 and F2) are obtained from Lahsen and Trujillo (1976) and Marinovic and Lahsen (1984). Fig. S1 shows the location of additional TEM stations along the selected profiles.

geothermal field suggest a N-S graben, where the geothermal field occupies the hanging wall (Lahsen and Trujillo 1976). This graben has been related to an extensional tectonic phase during the Pliocene (Tassi et al. 2010; Lahsen and Trujillo 1976). However, Lucchi et al. (2009) proposed that the structural pattern of El Tatio consists mainly of thrust faults largely striking NNE-SSW, intersected by local NW-SE trending lineaments.

Most of geothermal manifestations in El Tatio are distributed along three basins: The Upper, Middle and Lower Basin (Glennon and Pfaff, 2003). Here, we focus on the Upper Basin (UB) and the Middle Basin (MB), which are two largest (Fig. 1). The Upper Basin (UB) contains the largest number of geysers and erupting springs on a sinter platform. They are distributed in a preferential NE to SW alignment, parallel to the normal fault that limits the El Tatio graben proposed by Lahsen and Trujillo (1976). The Middle Basin (MB) corresponds to a flat sinter plain characterized by an alignment of mostly perpetual spouters in a NW-SE direction. Parallel to this orientation, Lahsen and Trujillo (1976) inferred a strike-slip fault (F2 in Fig. 1).

The El Tatio area is characterized by volcanic units from the Late Cenozoic to present, including stratovolcanoes and lava domes, as well as ignimbrite sheets related to the APVC (Glennon and Pfaff, 2003; Lucchi et al. 2009). Almost all lithological units are pyroclastic deposits or volcanic/subvolcanic bodies, associated with Neogene and Quaternary eruptions (Lahsen 1969; Marinovic and Lahsen 1984). The main units observed in stratigraphic order from oldest to youngest in the El Tatio area are the Pliocene Puripicar Ignimbrite (Cusicanqui 1975), Pliocene-Pleistocene Tucle formation, Pleistocene El Tatio Ignimbrite and Holocene/Late Pleistocene sands/gravels of glacial origin (Munoz-Saez et al. 2020). Three sets of volcanoes and lava of different ages which outcrop in the area are identified by Marinovic and Lahsen 1984: Miocene volcanic group I, Pliocene volcanic group II, and Pleistocene volcanic group III (Fig. 1). The Copacoya Dome is part of the first unit and corresponds to a 7.35 Ma dome of dacitic composition (Marinovic and Lahsen 1984).

The boreholes drilled in the area provided significant data to constrain the geology and hydrogeology of the El Tatio geothermal field, but only a few samples from the wells were described in detail in an internal report from the Empresa Nacional de Geotermia (ENG-FCFM, 2008). At depths <200 m, there are three main lithologies: quaternary deposits (sandstones and gravels), the Tucle tuff, and the El Tatio Ignimbrite. The borehole data also describe the presence of mineral alteration (e.g., quartz, illite, illite-montmorillonite and nontronite) by using XRD in two samples at 123 m and 256 m of depth, in wells P1 and P2, respectively. But these samples have no description of the shallow sinter deposits. A deep (> 600 m) and hot (260 to 270 °C) aquifer was found by the geothermal wells. This is located in the Puripicar and Salado ignimbrites, and confined by the impermeable Tucle tuffs. A shallower (200-250 m depth) and cooler (160 to 170 °C) aquifer was formed in the Tucle dacite, which is confined by the impermeable El Tatio ignimbrite (e.g., Cusicanqui 1975; Giggenbach 1978). Both aquifers occur at depths greater than those analyzed in our study. The boreholes do not provide specific information about the local meteoric water and depth of the water table.

## 2.2. Electrical resistivity in geothermal fields

High enthalpy geothermal systems present great variations in their resistivity/conductivity structure. The presence of high electrical conductivities is not only related to the occurrence of fluids, but also the presence of hydrothermal alteration minerals (Arnason et al., 2000; Munoz 2014; Oskooi et al., 2005). The presence of saline fluids is characteristic of geothermal systems (Nicholson 2012), which increases the electrical conductivity. The presence of fresh or meteoric water in rocks results in enhanced electrical conductivity too, although it has lower conductivity than saline water. Dry volcanic rocks usually have high resistivities, but water saturation or the presence of alteration

minerals can significantly reduce its electrical resistivity. It is difficult to differentiate saline water or alteration minerals using only electrical resistivity data. High enthalpy geothermal systems have been widely studied using geophysical methods which image the subsurface electrical resistivity (e.g., Arnason et al., 2000; Heise et al., 2008; Manzella et al., 2010; Oskooi et al., 2005; Ussher et al. 2000; Cumming and Mackie 2010). In general, electrical resistivity surveys can identify 3 important areas: the shallow superficial layer of undisturbed rock at temperatures below 70 °C with resistivities >100 Ωm; the low resistivities layer <10 Ωm, associated with impermeable clay minerals (e.g., smectite); and usually below, there is a permeable zone that corresponds to the geothermal reservoir. The reservoir shows high resistivities (10–60 Ωm) due to the formation of resistive alteration minerals (e.g., illite) at temperatures higher than 200 °C (e.g., Munoz 2014; Ussher et al. 2000). The depths of these structures can vary for each geothermal field. Figueroa (2019), using the magnetotelluric method, mapped the electrical resistivities around El Tatio in an area of ~20 km<sup>2</sup>, reaching up to depths of 5 km. This survey describes the two deep aquifers by identifying impermeable and altered zones/layers.

## 3. Methodology

The TEM method consists of a loop source and a loop receiver. An inductively ungrounded wire is used as the source, while an induction coil is used as the receiver to record the time derivative of the secondary magnetic field. The resolution of the upper layer and the depth of exploration of the TEM method depend primarily on the loop size and transmitted current. Below, we provide details of the configuration used in this study.

### 3.1. Survey setup and data acquisition

To model the electrical resistivity structures and observe the main differences between the Middle Basin (MB) and the Upper Basin (UB), a total of 5 TEM profiles were collected: 2 crossing the UB, 2 crossing the MB and 1 in the transition between both basins. The TEM profiles A, B and C were oriented in NW-SE direction and crossed the fault bounding the UB and MB (F1). Profiles D and E were located within the MB and bounded to the west by the strike slip fault F2 (Fig. 1). These profiles crossed the main geological formations, fault zones and therefore, possibly the areas of fluid ascent associated with geothermal surface manifestations. The target depth was roughly 150 m which required a relatively small, 40 m × 40 m square central loop transmitter. In total, we collected 50 TEM soundings. To acquire dense data, the spacing between the center of each sounding was 40 m. The measurements were done with the ABEM WalkTem instrument. At each station 3 full measuring cycles were realized, which correspond to approximately 600 stacks. For the early time recording we used a low moment with a current of 1 A to acquire data between  $t \sim 1 \mu\text{s}$  and  $t \sim 1 \text{ ms}$ . The high moment acquisition mode has a better signal to noise. It uses currents up to 7 A and obtains deep late time TEM data with a maximum recording time of ~25 ms.

### 3.2. Data processing, 1D inversion and 2D modeling

Stacked transients and error estimated for low moment and high moment data were obtained by calculating the mean and standard deviation of all stacks. The late time measurement errors were around 20%, affected by electromagnetic noise. We removed data with larger errors prior to the inversion.

The low and high moment transients had a current switch-off ramp of 5 and 7  $\mu\text{s}$ , respectively. Both transients were merged into one single transient. The data set of low moment was used for early times, while the high moment was used for the late times because a higher moment allows a deeper penetration and generates a better signal/noise ratio at late times (Danielsen et al. 2003; Sørensen and Auken, 2004; Auken et al.

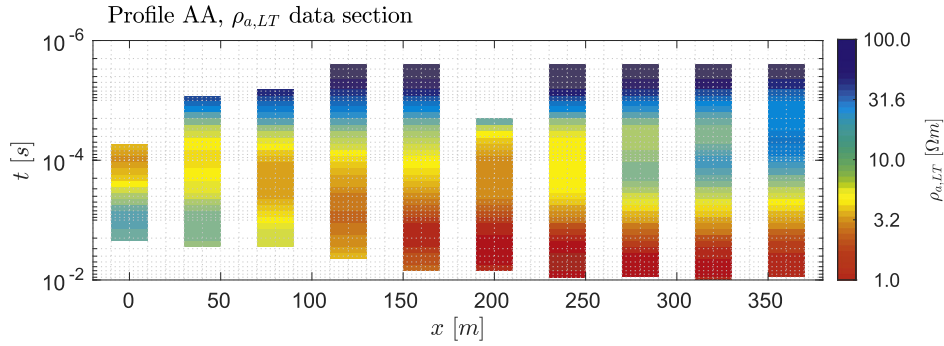


Fig. 2. Field data obtained along the profile AA' as color-coded pseudosection using the apparent resistivity late time ( $\rho_{a,LT}$ ) transformation (Spies and Frischknecht, 1991).

2006). To account for systematic errors, we set a minimum error floor of 2% (e.g., Yogeshwar et al. 2013). Fig. 2 displays the data obtained along profile AA' as a color-coded pseudosection using the apparent resistivity late time ( $\rho_{a,LT}$ ) transformation (Spies and Frischknecht, 1991). At the location of the fault, we observe a strong change in the data (left side of the profile).

In the first step, a conventional 1D inversion technique was used to evaluate the TEM data. We refer to Yogeshwar et al., 2020 for details on the inversion algorithm which was used. The algorithm allows different approaches: (1) The Marquardt-Levenberg (ML) technique to obtain models with a limited number of layers and discrete boundaries. (2) An Occam-type inversion with smoothness constraints and two different roughness criteria. Roughness R1 minimized the resistivity contrast between neighboring layers, and R2 the resistivity curvature to be small (Constable et al., 1987a,b). As the ML technique depends strongly on the starting model, these were constructed based on Occam inversion results. Typically, 3–5 layers were sufficient to explain the field data.

The misfit of the data was calculated using an error weighted relative root mean square (here termed  $\chi$ ).

$$\chi = \sqrt{\frac{1}{N} \sum_{i=1}^N \frac{(d_{obs,i} - d_{calc,i})^2}{\delta d_{obs,i}^2}} \quad (1)$$

A  $\chi = 1$  corresponds to an optimal data fit within the measurement errors.  $N$  is the number of data points,  $d_{obs,i}$  the  $i^{th}$  measured data,  $d_{calc,i}$  the  $i^{th}$  calculated data and  $\delta d_{obs,i}$  the measurement error. A global  $\chi$  is obtained by averaging the misfit along each complete profile.

In the following, we will present only the derived ML models, as we expect reasonably distinct resistivity contrast between the layers of the model, e.g., between background and conductive layer. In sedimentary environments a smooth model can be geologically more meaningful.

In many TEM case studies the 1D interpretation has proved to be feasible. However, significant inaccuracies can occur when the geological structures are multidimensional (Goldman et al. 1994). To avoid misinterpretation, we used a 2D forward modeling approach in the second step of our study to analyze the field data and validate the 1D inversion models. Fig. 3A displays a simple 2D forward model that considers a conductive truncated layer. The 2D response for an example sounding

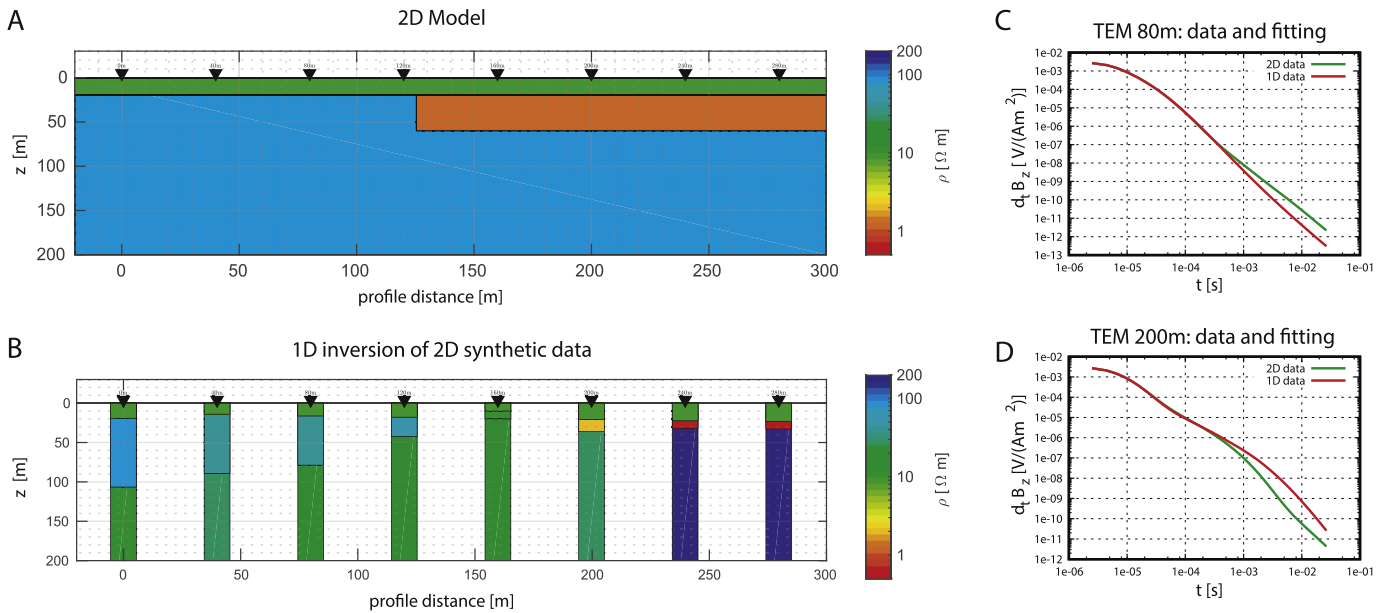


Fig. 3. Synthetic 2D forward model and the 1D inversion models of 2D data. The model corresponds to a layer of 20 m depth and 10  $\Omega m$  of resistivity, a truncated conductive layer of 40 m depth and 1  $\Omega m$  of resistivity and a background of 100  $\Omega m$ . A) 2D forward model considering a conductive truncated layer. Model based on the structures observed in the models on the upper basin profiles. B) 1D inversion models of the synthetic data obtained from 2D forward of model show in A. C) Example of the 2D synthetic data and 1D inversion response from a station located at 80 m along the profile. D) Example of the 2D synthetic data and 1D inversion response from a station located at 200 m along the profile. The study shows significant differences in the data obtained by 1D/2D model and bad representation of the model reproduced by 1D inversion in a 2D case.

located at the left of the truncated conductor (Fig. 3C) shows a decelerated voltage decay. This is because of the electrical current prevailing in the conductive layer. While on the right side of the truncated layer, the results are the inverse (Fig. 3D). The 1D inversion results along the complete profile using 2D simulated data results in an incorrect subsurface model (Fig. 3B). A false deep conductor is produced at the soundings located left of the conductor and the resistivity of half-space on the right side is overestimated. This simple study demonstrates the significance of using 2D interpretation techniques to avoid miss-interpretations.

The 2D TEM forward models were computed using the well-established time domain finite difference algorithm SLDMem3t (Druskin et al., 1999). The following three steps were used for our modeling approach:

(1) A 2D model was derived for each profile based on stitched 1D ML models. Each 2D model column was 40 m wide and located beneath each sounding. The model was extended to infinity in the strike direction.

(2) A 2D forward model was performed and the misfit of each sounding was calculated using eq. (1). To gain information about data not well fitted, which correspond mostly to deep or shallow zones, we calculated the relative percentage difference for each transient time point at each sounding.

$$RD_{field-2D} = \frac{V_{field} - V_{2D}}{V_{field}} \cdot 100 \quad (2)$$

Where  $V_{field}$  corresponds to the voltage data measured,  $V_{2D}$  to the 2D forward data. An  $RD < 0$  indicate that  $V_{2D} < V_{field}$ , while  $RD > 0$  indicate that  $V_{2D} > V_{field}$ .

(3) In this step we evaluated the resulting misfit of the 2D models. If the data was fitted equally well as by the 1D inversion results, we concluded that the 1D interpretation was adequate and can be relied on. In cases where data fit became much worse, the 2D model was altered and the forward simulation was repeated. Based on eq. (2), those zones of the 2D model corresponding to systematic poor data fit were modified.

## 4. Results

### 4.1. Comparison of 1D and 2D models

1D inversion modeling results are optimally fitted ( $\approx 1$ ) at most stations, however some profiles showed strong lateral electrical resistivity variations (e.g., profile AA', Fig. 4). Fig. 4A shows the model obtained by 1D ML inversion and Fig. 4B displays the relative differences between the 1D inversion results and field data, showing an optimal fit of  $=0.96$ . Nevertheless, the 2D forward results obtained by the same model results in a significantly increased data fit ( $\chi = 4.17$ ), which indicate that a lateral variation of resistivity has a significant impact on the soundings, and the 1D inversion might produce a misleading interpretation. It is striking that similar to the simple 2D modeling study shown in Fig. 3, a deep conductor is placed below sounding T23 to T25 and the slight thinning of the shallow conductor between T25 to T27, these could be caused by a 2D effect. The 2D model of profile AA' was modified and the best fitted (Fig. 4D) model was obtained when removing the conductor between T23 to T25 and modifying the shallow layer. These main modifications improve the 2D global fit considerably ( $\chi = 2.31$ ) and for most soundings (Fig. 4F), which can be observed in 2 exemplary stations (T24 and T26) on Fig. 4G.

A similar study was performed along profile BB' (Fig. S2). The best fitted model was obtained by modifying the resistivity structure of C3 below soundings T4 and T5. As for profile AA', the modified 2D forward model improved the data fit. The 1D inversion results along profiles CC', DD' and EE' did not show strong lateral variations of the resistivity. Consequently, in the case of these profiles the 2D forward models were fitted well ( $\chi = 1.64$ ,  $\chi = 1.50$  and  $\chi = 1.66$  respectively).

### 4.2. Result from 2D models

The following nomenclature is used in this section: HC for highly conductive bodies (resistivities  $< 3 \Omega\text{m}$ ); C for conductive bodies ( $3\text{--}30 \Omega\text{m}$ ); LR for low resistive bodies ( $30\text{--}100 \Omega\text{m}$ ); HR for highly resistive bodies ( $> 100 \Omega\text{m}$ ). The structures identified on the models have been named by the resistivity nomenclature and a number depending on their interpretation.

Along profile AA' (Fig. 5A), we observe four important zones: a shallow (20–60 m depth) highly conductive structure HC1 (resistivities between 0.5 and 2.5  $\Omega\text{m}$ ) whose thickness decreases towards the west; it is underlain by a more resistive LR3 layer with resistivities over 50  $\Omega\text{m}$  extending below soundings T27 to T32; a second conductive structure C2 at the northwest side of the profile with resistivities between 5 and 10  $\Omega\text{m}$  below T24–T26; and a highly resistive zone HR4 is observed below T23, with a resistivity value of approximately 250  $\Omega\text{m}$ . Although the C2 structure is observed more clearly in the 1D model because of the contrast with the adjacent sounding, we consider the 2D model to better represent the true resistivity structure. Profile BB' (Fig. 5B), presents similar structures compared to profile AA': the conductor HC1 with resistivities less than 3  $\Omega\text{m}$  and 20–60 m depth, a less conductive layer C3 (resistivities of 5–30  $\Omega\text{m}$ ) below T4–T9 and a conductive zone HC2 at the northwest side of the profile with resistivities between 1 and 2  $\Omega\text{m}$ . Profile CC' (Fig. 5C) shows a conductive layer HC1 with resistivities between 0.5 and 2  $\Omega\text{m}$  and 10–60 m depth, becoming more shallow towards the northwest. Underlying HC1 is a more resistive layer C3, but still quite conductive, with resistivities between 3 and 10  $\Omega\text{m}$ . In profile DD' (Fig. 5D), as in profile CC', a conductive layer HC1 (10–60 m depth) of resistivities between 0.8 and 1.5  $\Omega\text{m}$  is observed that overlaps a less conductive layer of resistivities that vary between 4 and 10  $\Omega\text{m}$  (C3). Finally, along the profile EE' (Fig. 5E), similar to profile CC' and DD', a conductive layer with resistivities between 0.8 and 1.3  $\Omega\text{m}$  is observed at 10–60 m depth, overlapping a less conductive layer C3 of resistivities between 8 and 13  $\Omega\text{m}$ .

The derived 2D models show two common features: HC1 which is a shallow ( $< 60$  m depth) very low resistivity body ( $< 3 \Omega\text{m}$ ) which extends laterally in all basins. It appears to be closest to the surface in areas with active geothermal manifestation; C3/LR3 which is a more resistive zone (but still considerably conductive) at depths  $> 50$  m below HC1. Furthermore, the shallowest layer (above HC1), varies in its resistivities along each profile. It is generally more conductive beneath the profiles CC', DD', and EE' with resistivities less than 10  $\Omega\text{m}$ . Along the profiles AA' and BB' it has resistivities  $< 10 \Omega\text{m}$  close to the geothermal manifestation, but they increase up to around 50  $\Omega\text{m}$  or more at the stations towards the east. In addition, there is a very shallow layer ( $< 3$  m) at the surface that is difficult to image due to the scale of the models. The TEM method cannot resolve such a shallow structure uniquely and the interpretation is uncertain. However, according to the well information (P1, P2 and P4), the most superficial layers corresponds to gravels and sandstones, which can highly differ in resistivity due to fluid content and/or hydrothermal alteration (an example of the comparison of the well's stratigraphy and 1D resistivity curve is shown in the supplementary material, Fig. S3).

## 5. Discussion

In the following sections we will discuss the obtained models shown in Fig. 5 with respect to geothermal and geological background information, considering the stratigraphy and alteration of nearby wells (ENG-FCFM, 2008).

### 5.1. Shallow conductor HC1

The shallow structure HC1, common in all the profiles, is stratigraphically correlated with sandstones and gravels that even when dry, are less resistive than dry volcanic rocks. Sandstones and

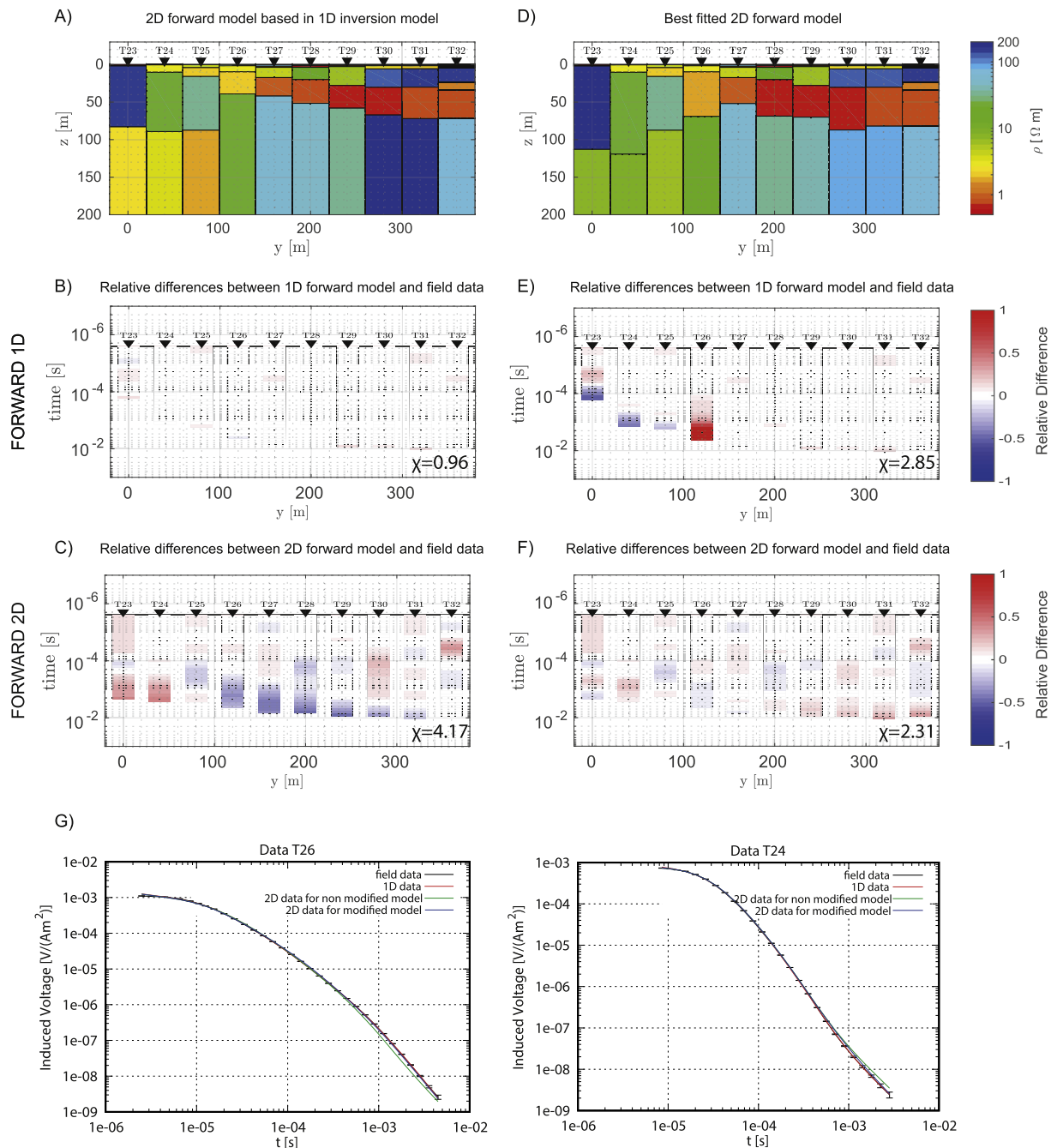


**Fig. 4.** Example of 2D modeling approach for the profile AA'. A) 2D forward model based on 1D inversion models. B) Relative differences between 1D inversion model responses and field data. C) Relative differences between 2D forward model and field data. D) Altered and best fitted 2D model of profile AA'. E) Relative differences between 1D forward model based on D and the field data. F) Relative differences between best fitted 2D model and field data. G) Response curves of T26 sounding. H) Response curves of T24 sounding.

gravel are porous medium capable of sustaining liquid/fluid flow. HC1 is directly related with the presence of geothermal manifestations in the surface (Fig. 5) and in consequence to the presence of fluids.

The surface thermal waters in El Tatio showed high salinity and electrical conductivities (e.g., Giggenschbach 1978; Muñoz-Saez et al. 2018). Muñoz-Saez et al. (2018) determined that the electrical conductivity of the water is 10–20 mS/cm which corresponds to the electrical resistivity values of 1  $\Omega$ m and 0.5  $\Omega$ m. The high conductivity of HC1 can be associated to porous rock saturated with thermal conductive fluids. However, the presence of fluids alone, cannot explain the high conductivity of HC1. A simple exercise based on Archie's Law (Archie 1942), was performed to determine the resistivity of this layer (Fig. S4, eq.

(1) in Supplementary material). The cementation exponent varies between 1.3 and 2.0 for gravels (Archie 1942) and between 1.6 and 2.0 for sandstones (Pengra et al. 1999). Porosities for gravel and sands can be between 30% to 40% (Bear 2013). Considering these factors in addition to the resistivities of the thermal fluids, the extreme conductivity of our model (with 40% fluid-filled porosity) provides a lower-bound on the resistivity of HC1 of 1.7  $\Omega$ m, which is more resistive than the observed in several of the TEM stations (e.g., ~0.5  $\Omega$ m in T28-T30). A second test considered the conductivity of a two-phase effective medium proposed by Hashin and Shtrikman (1962), where the upper bound of effective conductivity of the rock describes the case that the conductive material is perfectly interconnected, which correspond to the lower



bound of effective resistivity (Fig. S5, eq. (2) in the Supplementary material). The results, similar to Archie's Law, shows that the lower bound of effective resistivity varies between 2.5 and 1.7  $\Omega\text{m}$  in the case of 30% to 40% of porosity. The existence of brines with Cl concentrations up to 185 g/l in the area (Cusicanqui 1975; Giggenbach 1978) could explain easily the resistivities of HC1, however those appeared only in discrete areas and are not reaching the surface.

The temperatures registered in the boreholes at depths of HC1 varies between 100 and 150 °C, which corresponds to an argillic alteration zone (Huenges and Ledru 2011), where the resistivities are between 1 and 10  $\Omega\text{m}$  (Ussher et al. 2000). Such type of alteration may explain the low resistivities of HC1 as well, however, there is no information available that validates the presence of clay minerals at depths of this layer.

The general range of low resistivities is similar to the observed in other geothermal systems such as Yellowstone National Park, USA (Bouligand et al. 2019), where high conductivities are dominated by hydrothermally altered and water saturated rocks. This suggests that the low resistivities that we observe in most of the profiles are dominated by both the presence of water and hydrothermal alteration of the rocks.

Munoz-Saez et al. (2018) proposed the existence of a shallow aquifer of local meteoric water that reaches the surface at the eastern end of profiles AA' and BB' forming a wetland in the UB. Our data is not showing a clear connection between HC1 and the wetland suggesting that HC1 is either unrelated to this meteoric aquifer or our method is not fine enough to resolve this connection. However, in the MB, the HC1 conductor becomes shallower on profiles CC', DD' and EE', suggesting that this aquifer can be connected to meteoric water. The water geochemistry in MB showed greater dilution of thermal waters with meteoric water compared to UB (Giggenbach 1978; Corтеcci et al. 2005; Munoz-Saez et al. 2018). HC1 may interact with the meteoric aquifer towards the surface in the MB, and therefore those waters are more susceptible to dilution. This could also explain the differences between the resistivities of HC1 observed in the UB, for example in profile AA' with zones of ~0.5  $\Omega\text{m}$ , in comparison with the profiles in MB with resistivities mostly around 1  $\Omega\text{m}$ .

### 5.2. Conductive deep layer C3/ Low resistive layer LR3

We found a relatively low resistivity layer (C3/LR3) that is stratigraphically correlated with the El Tatio Ignimbrite unit. This lithological unit has been described as an impermeable layer, and it is interpreted to be the confiner layer for a thermal aquifer located at ~250 m (Cumming et al. 2002; ENG-FCFM, 2008; Lahsen and Trujillo 1976; Lucchi et al. 2009). Rocks acting to cap hydrothermal reservoirs are usually highly altered resulting in an abundance of clays which increase the conductivity of rocks (Oskooi et al., 2005, 2016). XRD studies (ENG-FCFM, 2008) support the presence of alteration minerals at those depths.

The C3/LR3 (El Tatio ignimbrite) resistivities observed beneath the AA' profile differ from other profiles, possibly because electromagnetic methods do not have good resolution below a conductive layer, and therefore it is difficult to accurately resolve the thickness of HC1 and the resistivities of the last layer C3/LR3. However, the models show differences between the resistivities of the deeper layer observed in the north (LR3) and in the south (C3). Apparently, the resistivities of this unit tends to decrease towards the south, which may be explained by a greater fracturing in the southern zone. An increased fracturing implies a greater permeability of the rock, making it capable of storing more fluids that increase its conductivity and hydrothermal alteration.

Different fractures in the south of the field are observed transverse to the main fault F1 mapped by Lahsen and Trujillo (1976), for example, in one of the thermal manifestations near the CC' profile a fracture in the EW direction has been photographed (Fig. S6).

A SW-NE strike-slip fault (F2 in Fig. 1) has been mapped perpendicular to DD' and EE' profiles (Lahsen and Trujillo 1976). This fault could act as a preferential zone of ascent of the deepest fluids to the surface. It was expected that profile DD' and EE' would cross this fault, however its presence is not clearly distinguishable in the TEM data. In profile EE', the contrast in resistivity of C3 between T33-T34 and T35, could be an indication of the presence of the fault, as in profiles AA' and BB' (which cross-cut F1). Thus, the models show a possible pathway for fluids to ascend from deeper aquifers.

### 5.3. High resistive body HR4

Another important zone observed on the AA' profile (Fig. 5A) is the most resistive structure (HR4) to the northwest, below T23. This area is geologically correlated with the El Tatio Ignimbrite and the presence of the Copacoya Dome, a dacitic dome of Miocene age. Below T23, there are two very thin layers that cannot be visualized in the models due to the axis scale. A 50  $\Omega\text{m}$  layer overlies a 0.3  $\Omega\text{m}$  layer here, but both are only 1 m thick. The first one probably corresponds to a shallow layer of the El Tatio Ignimbrite. However, interpreting such thin layers using TEM is difficult as they are at the limit of its resolution. Copacoya Dome has been described as an impermeable layer that would act as geological barrier to the waters flowing from the east, impeding its flow to the west and forcing them to ascend to the surface (e.g., Figueroa 2019), which is coherent with the resistivity of the body HR4. The resistivities of the dome are coherent with the resistivities found in other regional studies (e.g., Cumming and Mackie 2010; Figueroa 2019; Healy and Hochstein 1973; Lahsen and Trujillo 1976).

The high resistivity of HR4 is also consistent with resistivities observed outside of geothermal areas such as at Yellowstone National Park (e.g., Bouligand et al. 2019). However, the resistivity of HR4 is around 250  $\Omega\text{m}$  which is lower than those observed in Yellowstone, which are reported to be >1000  $\Omega\text{m}$  (e.g., Bouligand et al. 2019). The equivalent models for sounding TEM 23 in Fig. S7 show a wide range for the resistivities, indicating a structure of poor resolution. The TEM methodology has a better resolution for conductors than for resistors, and therefore, HR4 could have a much higher value and is interpreted to be outside the boundary of the geothermal area.

### 5.4. C2/HC2 connection of shallow and deep conductor

An important feature observed on the UB profiles (Fig. 5A and B) is the conductor C2/HC2, which is directly connected with the shallow conductive layer HC1 at the surface. C2/HC2 is stratigraphically correlated with the El Tatio Ignimbrite and spatially correlated with the presence of the F1 fault (Fig. 1). The high conductivity of C2/HC2 (especially apparent on BB') suggests the presence of a permeable zone that allows the ascent of fluid from hotter and deeper aquifers (200 m and 600 m). C2/HC2 is interpreted as the structure that feeds the aquifer HC1 with deep geothermal fluids. The presence of fluids in the zone would significantly reduce the resistivity of the ignimbrite, giving high lateral resistivity contrast with the other part of the ignimbrite C3/LR3.

Electromagnetic geophysical studies in other areas of the world have been useful to define fault zones distinguishing different stratigraphic units as zones of different resistivity, even being able to observe quantifiable vertical displacements of some formations (Suzuki et al. 2000;

**Fig. 5.** Best fitted 2D forward electrical resistivity models together with their geological interpretation for each profile. Segmented lines show the depth of investigation (DOI) (Spies 1989). The surface location of geothermal manifestations (Munoz-Saez et al. 2018) and stratigraphy of the boreholes are marked with symbols. Faults described in Fig. 1 are marked as F1 and F2. Red arrows indicate fluid ascent areas. Black solid lines delimit interpreted bodies.

Yogeshwar and Tezkan 2017). Along the profiles AA' and BB' a change in the thickness of HC1, that corresponds to quaternary deposits, is observed (between T25 and T26 for profile AA' and between T3 and T4 for profile BB'), which becomes thinner towards the north-west. This abrupt change in sediment thickness could be associated with the presence of a fault, but it would be difficult to make conclusions about the fault geometry or its kinematics. In El Tatio, a normal fault F1 (see Fig. 1) with vergence towards the SE in the UB has been mainly inferred by the topography, the alignment of geothermal manifestations and invoking an extensive regional regime (Lahsen and Trujillo, 1976). On the other hand, Lucchi et al. (2009) proposed that this area is mainly dominated by thrusting. The profile BB' shows C2/HC2 dipping in direction NW that would be incompatible with a normal fault of vergence SE. However, with the methods used in this study, we are able to observe only the shallow part of the system and not the fault geometry in depth.

In the Solfatara Plateau Thermal Area and Old Faithful in Yellowstone National Park, the ascent of fluids is associated with areas of weakness due to the contact between two lithological units (Bouligand et al. 2019; Wu et al. 2017). In El Tatio, C2/HC2 can indicate a weak zone associated to the lithological contact in depth between the Copacoya dome (HR4 in AA' discussed above) and the sequences of ignimbrites (Fig. 1). Even though the presence of the fault F1 is commonly invoked (e.g., Cusicanqui 1975; Lahsen and Trujillo, 1976; Munoz-Saez et al. 2018), thermal fluids could also ascend through this lithological contact without having a fault in the area. On the other hand, the properties of younger rocks are typically more heterogeneous compared to older rocks that have been highly indurated and are therefore more likely to produce fracture networks (Cumming 2016). A network of fractures in the El Tatio ignimbrite is also a possibility that would provide the necessary permeability for the ascent of fluids.

### 5.5. Summary of the local conceptual model

A conceptual model of UB and MB is summarized in Fig. 6. The thermal fluids move from east to west in the deeper aquifer (>200 m). In UB (Fig. 6A) the fluids ascend from the deeper aquifers through a permeable zone, here named C2/HC2. This area could be related to the presence of F1 fault, the lithological contact between two units, or a fracture network, however, it is difficult to clarify this with our dataset. Specifically in profile AA', the fluids flowing westward through deep aquifers encounter a geological barrier corresponding to the resistive anomaly HR4, associated with the Copacoya impermeable dome, which forces fluids to ascend. The El Tatio Ignimbrite and Tucle Tuffs are the confining layers of the deepest aquifer. They are highly hydrothermally altered, so C3/LR3 has high conductivity.

In the MB (Fig. 6B), profiles CC', DD' and EE' have similar characteristics without any clear zones of fluid ascent as in the UB. For interpretation, we consider the area around CC' as part of the MB. A shallow conductive layer HC1 and the surface layer appears to be more conductive in areas with perpetual spouters. The geochemistry of thermal waters (Munoz-Saez et al. 2018), indicates a larger mixture of deep mature waters with local young waters in the MB. HC1 is closer to the surface in the MB than in the UB, and it could be associated with a connection between the thermal and meteoric water in the shallow subsurface. Similar to profile EE', a contrast of C3 between T53-T54 adjoining soundings (T52 and T55) could indicate the presence of ascending fluids zone and then a permeable zone.

The previous conceptual model presented by Munoz-Saez et al. (2018) indicates the existence of the shallow meteoric aquifer HC1. However, we interpret HC1 as a thermal aquifer, which is connected to the shallow meteoric water at the surface in the MB. The resistivities of hydrothermal alteration minerals such as clays dominate over the

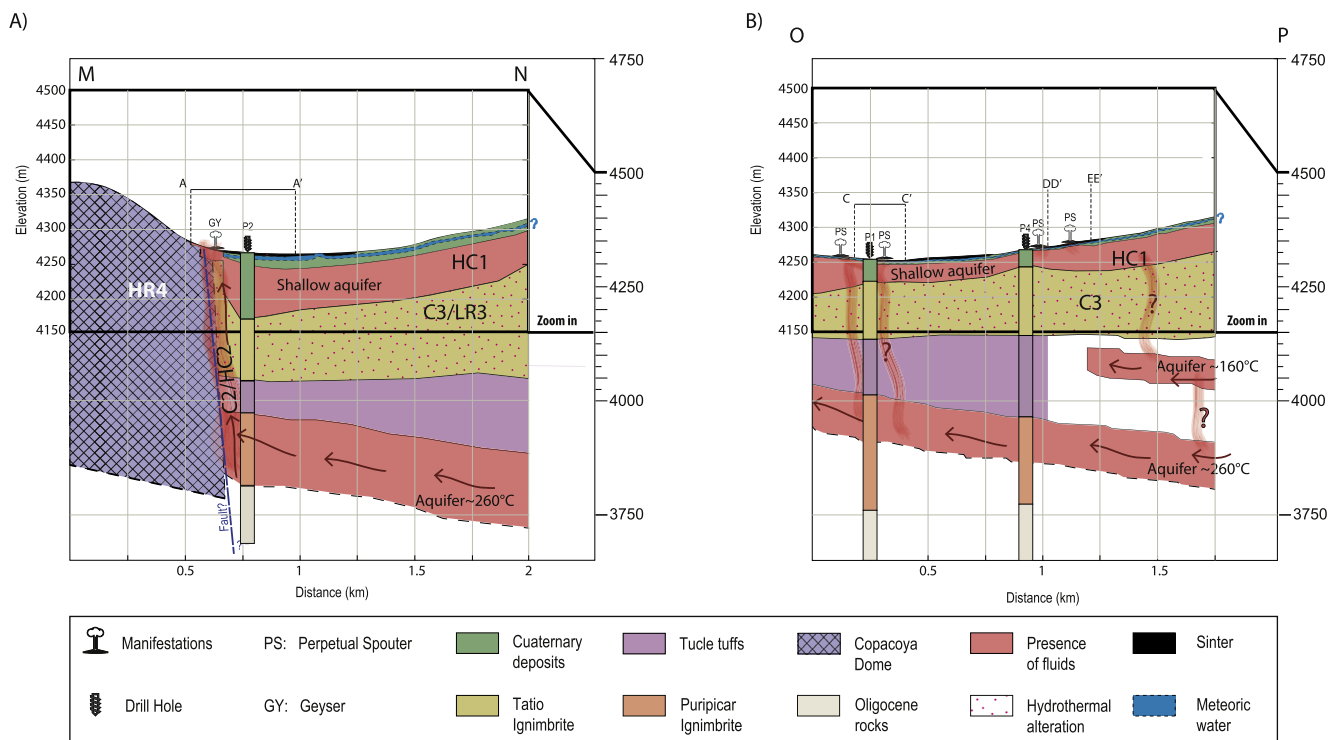


**Fig. 6.** Conceptual model of the El Tatio geothermal field that integrates the previously existing information and that obtained in this study. Depths are approximated and the model reaches to higher depths than our study, so we present a zoom in that allows us to observe the depths covered by the TEM models in more detail (black solid box). The model considers the location of geothermal manifestations (Munoz-Saez et al. 2018) and stratigraphy of the boreholes. A) Upper Basin: The thermal fluids move from east to west in the deeper aquifer (>200 m). The impermeable geologic barrier associated with the Miocene Copacoya dome forces the ascent of fluids from the deeper aquifers to the shallow aquifer HC1 through a permeable zone (C2/HC2). HC1 is the direct feeder of the geothermal manifestations. B) Middle Basin: Has similar characteristics as Upper Basin but there is no resistive and impermeable structure acting as a barrier, and zones of ascending fluids are not imaged as in the Upper Basin.

chemistry of the reservoir fluids, so it is not possible to differentiate the type of fluids that HC1 contains with our models. Nonetheless, the direct connection of C2/H2 with HC1 indicates that HC1 may be fed by deeper aquifers, as explained in section 5.2. In addition, Munoz-Saez et al. (2018) propose that the wetlands of the UB occurs when the water table reaches the surface, but we do not observe that HC1 become more superficial in the wetland areas, for example beneath the profile BB' which crosses the wetland. Therefore, we propose that the fluids present in HC1 correspond predominately to thermal fluids, interacting only locally with meteoric water.

We observed structural differences between the UB and MB, which could be affecting the type of geothermal manifestations existing in each basin. Nevertheless, it is not possible to draw a conclusion from our data. The influence of the underground geometry and the presence of cavities and ducts have been described as an important factor in the dynamics of geysers (e.g. Belousov et al. 2013; Vandemeulebrouck et al. 2013; Ardid et al. 2019; Wu et al. 2017). These cavities at El Tatio are located at depths <20 m (Munoz-Saez et al. 2015; Ardid et al. 2019) and we are not able to resolve these geometries with our data.

## 6. Conclusions

This TEM study has yielded, for the first time, an electrical resistivity model of the shallow structures beneath the El Tatio geothermal field. Five profiles crossing two of the most important basins (Middle and Upper basins) were analyzed. The 2D resistivity models contained conductive features with resistivity values which were consistent with the low resistivity values usually found in highly altered geothermal areas with large quantities of high temperature circulating saline fluids.

As a common feature in all profiles, a very low resistivity zone HC1 (< 3  $\Omega$ m) was detected at depths up to 60 m. This structure coincides with a unit of quaternary deposits. Due to its permeability and high conductivity, it was interpreted as a superficial aquifer containing saline thermal water which feeds geothermal manifestations at the surface. A second common feature (C3/LR3) has been imaged and, although still conductive, is more resistive than HC1. C3/LR3 corresponds stratigraphically to the El Tatio Ignimbrite, which is highly hydrothermally altered and likely represents an impermeable zone that confines the deeper thermal aquifer (>200 m). It has low resistivities between 5 and 10  $\Omega$ m in most cases.

Structural differences were identified between the profiles located in the Upper Basin and the Middle Basin. A high conductivity zone (C2/HC2) is observed in the Upper Basin, which has been interpreted as a permeable zone that allows the ascent of fluids from deep thermal aquifers (>200 m) to the shallow aquifer HC1. In addition, beneath the profile AA' a highly resistive zone was identified to the NW that is interpreted as an impermeable geological barrier, correlated with the Copacoya dome, that impedes the westward fluid flow. In the Middle Basin, the exact pathways through which hot fluids move from deep aquifers to CH1 are uncertain, but small changes in conductivity can be related to a strike-slip fault present in the area. This work suggests that a shallow aquifer containing thermal waters (HC1) exists beneath El Tatio geothermal field. This shallow thermal aquifer has not been described before and this new information will help improve the current conceptual model of El Tatio geothermal field.

## CRedit authorship contribution statement

**Daniela Montecinos-Cuadros:** Conceptualization, Funding acquisition, Data curation, Methodology, Software, Writing - original draft, Writing - review & editing. **Daniel Díaz:** Conceptualization, Funding acquisition, Data curation, Methodology, Writing - original draft. **Pritam Yogeshwar:** Methodology, Software, Data curation, Writing - original draft, Writing - review & editing. **Carolina Munoz-Saez:** Data curation, Writing - original draft, Writing - review & editing.

## Declaration of Competing Interest

The authors declare that they have no known competing financial interests or personal relationships that could have appeared to influence the work reported in this paper.

## Acknowledgments

This work has been funded by Andean Geothermal Center of Excellence (CEGA), project FONDAP 15090013. We thank the support from PIA/CONICYT Anillo ACT-172002. The co author Dr. Munoz-Saez was supported the American Association for University Women Postdoctoral Grant.

We would also like to thank Ariel Figueroa, Gustavo Perez, Felipe Reyes, Felipe Zuñiga, Renzo Mancini and María José Hernandez for their fieldwork assistance; the Toconce and Caspana communities for their permission to conduct this study in the El Tatio geothermal field; and to Darcy Cordell for his valuable comments which helped us to improve the manuscript. Finally, we thank the two anonymous reviewers from JVGR for all their constructive comments that greatly improved the quality of the manuscript.

The original data used in this work are available for reproduction and are freely accessible at the following link: [https://osf.io/6pu4m/?view\\_only=6af092f178ce42299cad08502eb654e4](https://osf.io/6pu4m/?view_only=6af092f178ce42299cad08502eb654e4)

## Appendix A. Supplementary data

Supplementary data to this article can be found online at <https://doi.org/10.1016/j.jvolgeores.2021.107198>.

## References

- Archie, G.E., 1942. The electrical resistivity log as an aid in determining some reservoir characteristics. *Trans. AIME* 146 (01), 54–62.
- Ardid, A., Vera, E., Kelly, C., Manga, M., Munoz-Saez, C., Maksymowicz, A., Ortega-Culaciati, F., 2019. Geometry of geyser plumbing inferred from ground deformation. *J. Geophys. Res. Solid Earth* 124 (1), 1072–1083.
- Arnason, K., Eysteinnsson, H., Hersir, G.P., 2010. Joint 1D inversion of TEM and MT data and 3D inversion of MT data in the Hengill area, SW Iceland. *Geothermics* 39 (1), 13–34.
- Arnason, K., Karlsdottir, R., Eysteinnsson, H., Flovenz, O.G., Gudlaugsson, S.T., 2000. The Resistivity Structure of High-temperature Geothermal Systems in Iceland. pp. 923–928.
- Auken, E., Pellerin, L., Christensen, N.B., Sørensen, K., 2006. A survey of current trends in near-surface electrical and electromagnetic methods. *Geophysics* 71 (5), G249–G260.
- Bear, J., 2013. *Dynamics of Fluids in Porous Media*. Courier Corporation.
- Belousov, A., Belousova, M., Nechayev, A., 2013. Video observations inside conduits of erupting geysers in Kamchatka, Russia, and their geological framework: Implications for the geyser mechanism. *Geology* 41 (4), 387–390.
- Bouligand, C., Hurwitz, S., Vandemeulebrouck, J., Byrdina, S., Kass, M.A., Lewicki, J.L., 2019. Heat and mass transport in a vapor-dominated hydrothermal area in Yellowstone National Park, USA: Inferences from magnetic, electrical, electromagnetic, subsurface temperature, and diffuse CO<sub>2</sub> flux measurements. *J. Geophys. Res. Solid Earth* 124, 291–309.
- Constable, S.C., Parker, R.L., Constable, C.G., 1987. Occam's inversion: a practical algorithm for generating smooth models from electromagnetic sounding data. *Geophysics* 52 (3), 289–300.
- Cortecchi, G., Boschetti, T., Mussi, M., Lameli, C.H., Mucchino, C., Barbieri, M., 2005. New chemical and original isotopic data on waters from el tatio geothermal field, northern Chile. *Geochem. J.* 39 (6), 547–571.
- Cumming, W., 2016. Resource conceptual models of volcano-hosted geothermal reservoirs for exploration well targeting and resource capacity assessment: construction, pitfalls and challenges. *Geotherm. Resour. Council Trans.* 40, 623–637.
- Cumming, W., Mackie, R., 2010. Resistivity imaging of geothermal resources using 1d, 2d and 3d mt inversion and tdem static shift correction illustrated by a glass mountain case history. *Proceedings World Geothermal Congress, Bali, Indonesia*, pp. 25–29.
- Cumming, W., Vieytes, H., Ramirez, C., Sussman, D., 2002. Exploration of the La Torta geothermal prospect, northern Chile. *Geotherm. Resour. Council Trans.* 26, 3–7.
- Cusicanqui, H., 1975. The geochemistry of the el tatio geothermal field, northern Chile. *Second United Nations Symposium on the Development and Utilization of Geothermal Resources, San Francisco*, 1975.
- Danielsen, J.E., Auken, E., Jørgensen, F., Søndergaard, V., Sørensen, K.L., 2003. The application of the transient electromagnetic method in hydrogeophysical surveys. *J. Appl. Geophys.* 53 (4), 181–198.
- De Silva, S.L., Self, S., Francis, P.W., Drake, R.E., Carlos, R.R., 1994. Effusive silicic volcanism in the Central Andes: the Chao dacite and other young lavas of the Altiplano-Puna Volcanic complex. *J. Geophys. Res. Solid Earth* 99 (B9), 17805–17825.

- Desclotres, M., Ritz, M., Robineau, B., Courteaud, M., 1997. Electrical structure beneath the eastern col-lapsed flank of Piton de la Fournaise volcano, Reunion Island: Implications for the quest for groundwater. *Water Resour. Res.* 33, 13–19.
- Dickey, K.A., 2018. Geophysical Investigation of the Yellowstone Hydrothermal System. Druskin, V.L., Knizhnerman, L.A., Lee, P., 1999. New spectral Lanczos decomposition method for induction modeling in arbitrary 3-D geometry. *Geophysics* 64, 701–706.
- ENG-FCFM, 2008. Estudio geológico del sector de el tatio (Reporte interno).
- Figueroa, A., 2019. Modelación geofísica del sistema geotermal el tatio-la torta (Tesis para optar al grado de magister en Ciencias, Mención Geofísica). Universidad de Chile.
- Fitterman, D.V., Stewart, M.T., 1986. Transient electromagnetic sounding for groundwater. *Geophysics* 51 (4), 995–1005.
- Giggenbach, W.F., 1978. The isotopic composition of waters from the el tatio geothermal field, northern Chile. *Geochim. Cosmochim. Acta* 42 (7), 979–988.
- Glennon, J.A., Pfaff, R.M., 2003. The extraordinary thermal activity of el tatio geyser field, Antofagasta region, Chile. *GOSA Trans.* 8, 31–78.
- Goldman, M., Tabarovsky, L., Rabinovich, M., 1994. On the influence of 3-d structures in the interpretation of transient electromagnetic sounding data. *Geophysics* 59 (6), 889–901.
- Goto, Y., Johmori, A., 2011. Controlled source audio-frequency magnetotelluric (csamt) and time domain electromagnetic (tdem) resistivity measurements at Noboribetsu geothermal field, Kuttara volcano, Hokkaido, Japan. *Bull. Volcanol. Soc. Jpn.* 56, 153–160.
- Gresse, M., Vandemeulebrouck, J., Byrdina, S., Chiodini, G., Revil, A., Johnson, T.C., Ricci, T., Vilardo, G., Mangiacapra, A., Lebourg, T., 2017. Three-dimensional electrical resistivity tomography of the Solfatara crater (Italy): implication for the multiphase flow structure of the shallow hydrothermal system. *J. Geophys. Res. Solid Earth* 122, 8749–8768.
- Hashin, Z., Shtrikman, S., 1962. A variational approach to the theory of the elastic behaviour of multiphase materials. *J. Mech. Phys. Solids* 11 (2), 127–140.
- Healy, J., Hochstein, M., 1973. Horizontal flow in hydrothermal systems. *N. Z. J. Hydrol.* 12, 71–82.
- Heise, W., Caldwell, T.G., Bibby, H.M., Bannister, S.C., 2008. Three-dimensional modelling of magnetotelluric data from the Rotokawa geothermal field, Taupo Volcanic Zone, New Zealand. *Geophys. J. Int.* 173, 740–750.
- Huenges, E., Ledru, P., 2011. Geothermal Energy Systems: Exploration, Development, and Utilization. John Wiley & Sons.
- Jousset, P., Haberland, C., Bauer, K., Arnason, K., 2011. Hengill geothermal volcanic complex (Iceland) characterized by integrated geophysical observations. *Geothermics* 40, 1–24.
- Kajiwara, T., Mogi, T., Fomenko, E., Ehara, S., 2000. Three-dimensional modeling of geoelectrical structure based on MT and TDEM data in Mori geothermal held, Hokkaido, Japan. *Proc. World Geothermal Congress, Kyushu-Tohoku, Japan*, pp. 1313–1318.
- Lahsen, A., 1969. Geología del área comprendida entre el tatio y los cerros de ayquina. Comité Geotérmico CORFO (internal report). pp. 1–75.
- Lahsen, A., Trujillo, P., 1976. El campo geotérmico de el tatio, Chile. *Proceedings: Second United Nations Symposium on the Development and Use of Geothermal Resources, San Francisco, California, USA, 20–29 May 1975*, 1, pp. 157–170.
- Lévy, L., Maury, P.K., Byrdina, S., Vandemeulebrouck, J., Sigmundsson, F., Arnason, K., Ricci, T., Deldicque, D., Roger, M., Gibert, B., 2019. Electrical resistivity tomography and time-domain induced polarization field investigations of geothermal areas at Krafla, Iceland: comparison to borehole and laboratory frequency-domain electrical observations. *Geophys. J. Int.* 218, 1469–1489.
- Lucchi, F., Tranne, C.A., Rossi, P.L., Gallardo, C., De Astis, G., Pini, G.A., 2009. Volcanic and tectonic history of the el tatio area (central andes, northern Chile): explanatory notes to the 1: 50,000 scale geological map. *Geoacta Spec. Publ.* 2, 1–29.
- Manzella, A., Ungarelli, C., Ruggieri, G., Giolito, C., Fiordelisi, A., 2010. Electrical resistivity at the Travale geothermal field (Italy). *Proceedings World Geothermal Congress, Bali, Indonesia*.
- Marinovic, N., Lahsen, A., 1984. Hoja calama: Región de antofagasta: carta geológica de Chile 1: 250.000. Servicio Nacional de Geología y Minería.
- Martínez-Moreno, F.J., Monteiro-Santos, F.A., Madeira, J., Bernardo, I., Soares, A., Esteves, M., Adão, F., 2016. Water prospection in volcanic islands by Time Domain Electromagnetic (TDEM) surveying: the case study of the islands of Fogo and Santo Antão in Cape Verde. *J. Appl. Geophys.* 134, 226–234.
- Mourguers, J.D., 2017. Modelación hidrogeológica de un sistema geotermal andino, aplicación en campo geotérmico el tatio, ii región de antofagasta. (Unpublished master's thesis). Universidad de Chile.
- Munoz, G., 2014. Exploring for geothermal resources with electromagnetic methods. *Surv. Geophys.* 35 (1), 101–122.
- Munoz-Saez, C., Namiki, A., Manga, M., 2015. Geyser eruption intervals and interactions: examples from el tatio, Atacama, Chile. *J. Geophys. Res. Solid Earth* 120 (11), 7490–7507.
- Munoz-Saez, C., Salties, S., Manga, M., Nguyen, C., Gonnermann, H., 2016. Physical and hydraulic properties of modern sinter deposits: El tatio, Atacama. *J. Volcanol. Geotherm. Res.* 325, 156–168.
- Munoz-Saez, C., Manga, M., Hurwitz, S., 2018. Hydrothermal discharge from the el tatio basin, Atacama, Chile. *J. Volcanol. Geotherm. Res.* 361, 25–35.
- Munoz-Saez, C., Manga, M., Hurwitz, S., Slagter, S., Churchill, D.M., Reich, M., et al., 2020. Radiocarbon dating of silica sinter and postglacial hydrothermal activity in the El Tatio geyser field. *Geophys. Res. Lett.* 47. <https://doi.org/10.1029/2020GL087908>.
- Nicholson, K., 2012. Geothermal fluids: Chemistry and exploration techniques. Springer Science & Business Media.
- Oskooi, B., Pedersen, L.B., Smirnov, M., Arnason, K., Eysteinnsson, H., Manzella, A., Group, D. W., 2005. The deep geothermal structure of the Mid-Atlantic Ridge deduced from MT data in SW Iceland. *Phys. Earth Planet. Inter.* 150, 183–195.
- Oskooi, B., Takalu, M., MonTahaiei, M., Rahmani, M.R., 2016. A recent magnetotelluric investigation of the Sabalan geothermal field in north-western Iran. *Bollettino di Geofisica Teorica ed Applicata*, p. 57.
- Pengra, D.B., Xi Li, S., Wong, P.-z., 1999. Determination of rock properties by low-frequency ac electrokinetics. *J. Geophys. Res. Solid Earth* 104 (B12), 29485–29508.
- Ruthsatz, A.D., Flores, A.S., Diaz, D., Reinoso, P.S., Herrera, C., Brasse, H., 2018. Joint tem and mt aquifer study in the Atacama desert, North Chile. *J. Appl. Geophys.* 153, 7–16.
- Sørensen, K., Auken, E., 2004. Skytem? A new high-resolution helicopter transient electromagnetic system. *Explor. Geophys.* 35 (3), 194–202.
- Spies, B.R., 1989. Depth of investigation in electromagnetic sounding methods. *Geophysics* 54 (7), 872–888.
- Spies, B.R., Frischknecht, F.C., 1991. Electromagnetic sounding. In: Nabighian, M.N. (Ed.), *Electromagnetic Methods in Applied Geophysics* (Vol. 2, pp. 285–426). Society of Exploration Geophysicists, Oklahoma City, OK.
- Suzuki, K., Toda, S., Kusunoki, K., Fujimitsu, Y., Mogi, T., Jomori, A., 2000. Case Studies of Electrical and Electromagnetic Methods Applied to Mapping Active Faults beneath the Thick Quaternary.
- Tassi, F., Aguilera, F., Darrah, T., Vaselli, O., Capaccioni, B., Poreda, R., Huertas, A.D., 2010. Fluid geochemistry of hydrothermal systems in the aricaparacota, tarapacá and Antofagasta regions (northern Chile). *J. Volcanol. Geotherm. Res.* 192 (1–2), 1–15.
- Tezkan, B., 1999. A review of environmental applications of quasi-stationary electromagnetic techniques. *Surv. Geophys.* 20 (3–4), 279–308.
- Tocchi, E., 1923. Studio geologico e geotermico del tatio cileno Reserved report to Larderello SA: Italy.
- Ussher, G., Harvey, C., Johnstone, R., Anderson, E., 2000. Understanding the resistivities observed in geothermal systems. *Proceedings World Geothermal Congress, Kyushu*, pp. 1915–1920.
- Vandemeulebrouck, J., Roux, P., Cros, E., 2013. The plumbing of Old Faithful Geyser revealed by hydrothermal tremor. *Geophys. Res. Lett.* 40, 1989–1993.
- Wu, S.M., Ward, K.M., Farrell, J., Lin, F.C., Karplus, M., Smith, R.B., 2017. Anatomy of old faithful from subsurface seismic imaging of the Yellowstone Upper Geyser Basin. *Geophys. Res. Lett.* 44, 10–240.
- Yogeshwar, P., Tezkan, B., 2017. Two-dimensional basement modeling of central loop transient electromagnetic data from the Central Azraq basin area, Jordan. *J. Appl. Geophys.* 136, 198–210.
- Yogeshwar, P., Tezkan, B., Haroon, A., 2013. Investigation of the Azraq sedimentary basin, Jordan using integrated geoelectrical and electromagnetic techniques. *Near Surf. Geophys.* 11, 381–389.
- Yogeshwar, P., Küpper, M., Tezkan, B., Rath, V., Kiyan, D., Byrdina, S., ... Viveiros, F., 2020. Innovative boat-towed transient electromagnetics—Investigation of the Furnas volcanic lake hydrothermal system, Azores. *Geophysics* 85 (2), E41–E56.